

# Domain Boundary Formation Within an Intercalated Pb Monolayer Featuring Charge-Neutral Epitaxial Graphene

Philip Schädlich, Chitran Ghosal, Monja Stettner, Bharti Matta, Susanne Wolff, Franziska Schölzel, Peter Richter, Mark Hutter, Anja Haags, Sabine Wenzel, Zamin Mamiyev, Julian Koch, Serguei Soubatch, Philipp Rosenzweig, Craig Polley, Frank Stefan Tautz, Christian Kumpf, Kathrin Küster, Ulrich Starke, Thomas Seyller, Francois C. Bocquet, and Christoph Tegenkamp\*

The synthesis of new graphene-based quantum materials by intercalation is an auspicious approach. However, an accompanying proximity coupling depends crucially on the structural details of the new heterostructure. It is studied in detail the Pb monolayer structure after intercalation into the graphene buffer layer on the SiC(0001) interface by means of photoelectron spectroscopy, x-ray standing waves, and scanning tunneling microscopy. A coherent fraction close to unity proves the formation of a flat Pb monolayer on the SiC surface. An interlayer distance of 3.67 Å to the suspended graphene underlines the formation of a truly van der Waals heterostructure. The 2D Pb layer reveals a quasi ten-fold periodicity due to the formation of a grain boundary network, ensuring the saturation of the Si surface bonds. Moreover, the densely-packed Pb layer also efficiently minimizes the doping influence by the SiC substrate, both from the surface dangling bonds and the SiC surface polarization, giving rise to charge-neutral monolayer graphene. The observation of a long-ranged ( $\sqrt{3} \times \sqrt{3}$ ) reconstruction on the graphene lattice at tunneling conditions close to Fermi energy is most likely a result of a nesting condition to be perfectly fulfilled.


## 1. Introduction

Extensive research has been carried out in the past to investigate the exceptional properties of graphene.<sup>[1,2]</sup> A step further in complexity involves combining different 2D materials to create novel quantum materials, such as superconducting graphene.<sup>[3,4]</sup> Among other approaches, the intercalation of elements on epitaxial systems, e.g., SiC(0001), is a versatile technique to synthesize well-defined interface layers with partly new properties and proximity-induced effects to graphene.<sup>[5]</sup>

A very important aspect in this context is the formation of quasi-freestanding monolayer graphene (MLG), which in case of epitaxially grown graphene necessitates an effective decoupling from the underlying substrate. One way to achieve this is intercalating the graphene layer

P. Schädlich, S. Wolff, F. Schölzel, P. Richter, T. Seyller  
Technische Physik  
Institut für Physik  
Technische Universität Chemnitz  
Reichenhainer Str. 70, 09126 Chemnitz, Germany  
P. Schädlich, S. Wolff, F. Schölzel, P. Richter, T. Seyller  
Center for Materials  
Architectures and Integration of Nano Membranes (MAIN)  
Technische Universität Chemnitz  
Rosenbergstr. 6, 09126 Chemnitz, Germany

C. Ghosal, Z. Mamiyev, J. Koch, C. Tegenkamp  
Analytik an Festkörperoberflächen  
Institut für Physik  
Technische Universität Chemnitz  
Reichenhainer Str. 70, 09126 Chemnitz, Germany  
E-mail: christoph.tegenkamp@physik.tu-chemnitz.de  
M. Stettner, M. Hutter, A. Haags, S. Wenzel, S. Soubatch, F. S. Tautz,  
C. Kumpf, F. C. Bocquet  
Peter Grünberg Institut (PGI-3)  
Forschungszentrum Jülich  
52425 Jülich, Germany  
M. Stettner, M. Hutter, A. Haags, S. Wenzel, S. Soubatch, F. S. Tautz,  
C. Kumpf, F. C. Bocquet  
Jülich Aachen Research Alliance (JARA)  
Fundamentals of Future Information Technology  
52425 Jülich, Germany  
M. Stettner, M. Hutter, A. Haags, S. Wenzel, S. Soubatch, F. S. Tautz,  
C. Kumpf, F. C. Bocquet  
Experimentalphysik IV A  
RWTH Aachen University  
52074 Aachen, Germany

 The ORCID identification number(s) for the author(s) of this article can be found under <https://doi.org/10.1002/admi.202300471>

© 2023 The Authors. Advanced Materials Interfaces published by Wiley-VCH GmbH. This is an open access article under the terms of the Creative Commons Attribution License, which permits use, distribution and reproduction in any medium, provided the original work is properly cited.

DOI: 10.1002/admi.202300471

with other elements. For our case, decoupling of graphene from the SiC(0001) substrate, various elements were successfully proven to be suitable and form (partly) well-defined interface structures with different functionalities.<sup>[6]</sup> For instance, intercalation of H results in full saturation of the dangling bonds at the interface, thus the intrinsic strong n-type doping is considerably reduced with improved charge carrier mobilities.<sup>[7,8]</sup> Contrary, the intercalation of Ca, Gd, or Yb causes strong doping and gives rise to electronic correlation effects opening the potential for unconventional superconductivity.<sup>[9–13]</sup> Intermediate doping scenarios have also been realized using Au, Ag, and Ge, resulting in metallic and semiconducting interlayers as well as p- and n-type doped epitaxial graphene layers.<sup>[14–18]</sup>

Possibly driven by the manifold of monolayer (ML) Pb structures on Si surfaces,<sup>[19]</sup> the intercalation of Pb into the interlayer of graphene and SiC has attracted attention in recent years.<sup>[20–27]</sup> Dense Pb ML structures, such as the striped incommensurate phase (SIC-phase) and the  $(\sqrt{7} \times \sqrt{3})$  reconstruction on Si(111),<sup>[28]</sup> have demonstrated 2D superconductivity.<sup>[29]</sup> Meanwhile, on Si(557), the deposition of a densely packed ML system revealed the formation of a spin-orbit density wave phase and 1D conductivity.<sup>[30,31]</sup> Achieving such transport signatures on SiC surfaces and in graphene would open fully new perspectives.

The wetting layer phase of Pb/Si(111) exhibits a diverse range of superstructures that vary from chain-like linear phases to hexagonal phases. This exceptional flexibility is known as the devil's staircase regime and spans from 1.20–1.33 ML.<sup>[28,32–34]</sup> Two distinct structural motifs, the  $(\sqrt{7} \times \sqrt{3})$  unit cell (UC) and the  $\alpha$ -Pb  $(\sqrt{3} \times \sqrt{3})$  UC, are responsible for generating these superstructures, corresponding to coverages of 6/5 ML and 4/3 ML, respectively. Two local structures, denoted as  $H_3$  and  $T_4$  have been proposed for the  $\alpha$ -Pb  $(\sqrt{3} \times \sqrt{3})$  reconstruction. As shown by density functional theory (DFT) calculations and Raman measurements, the total energies of these two structures differ by less than 10 meV per  $(1 \times 1)$  UC.<sup>[35–37]</sup> Consequently, mixtures of these structures may appear. The SIC-phase is an example of such a mixed phase thought to be composed of  $H_3$  and  $T_4$  domains. To what extent this flexibility is present on Si-terminated SiC(0001) surfaces, is unknown so far.

The intercalation of Pb between the carbon buffer layer (BL) and SiC(0001) depends on several factors, e.g., the defect concentration in the BL and an extremely complex energy landscape with many different energy barriers.<sup>[27]</sup> Thus, the final amount of intercalated material is difficult to control. In earlier experiments, hexagonally arranged bubble-like structures were reported.<sup>[20]</sup> More recently, both striped and hexagonally arranged patterns were reported and explained by a Moiré effect of the graphene layer with ML structures of Pb(110) and Pb(111), respectively, at the interface.<sup>[22]</sup> Own experiments have shown that multiple

adsorption-intercalation cycles can result in intercalation of 2–3 ML of Pb, where the topmost Pb layer revealed the honeycomb structure of plumbene in proximity to graphene.<sup>[26]</sup> Although DFT calculations suggest that Pb is acting as an electron donor, depending on the adsorption site and amount,<sup>[23]</sup> spectroscopy revealed a p-type doping of graphene, tending to suggest an acceptor behavior of Pb. For an intercalated Pb ML phase, an almost perfect charge-neutral graphene was reported.<sup>[25]</sup>

In this paper, we performed a structural analysis of the domain boundary formation of an intercalated Pb ML giving rise to charge-neutral epitaxial monolayer graphene on SiC(0001). We prove unambiguously that the single and closed packed Pb layer fits almost perfectly to the  $(1 \times 1)$  structure of the SiC(0001) lattice. However, residual strain at the interface within the Pb ML leads to the formation of a quasi-hexagonal grain boundary structure. Apparently, the densely-packed Pb ML saturates Si-dangling bonds and compensates or screens the SiC surface dipole. Interestingly, in STM (at low bias and temperature) the graphene exhibits a long-range ordered  $(\sqrt{3} \times \sqrt{3})$  reconstruction, resembling a Kekulé ground state, which seems to be induced by the scattering of Dirac electrons in the proximity of the grain boundaries.

## 2. Results and Discussion

### 2.1. Geometric Structure

An overview scanning tunneling microscopy (STM) image of an intercalated ML of Pb is shown in **Figure 1a**. Clearly visible are quasi-hexagonal and hexagonally-arranged structures. Most obvious, the center of the hexagons appear brighter and the edges form an irregular network. **Figure 1b** shows the corresponding spot profile analysis-low energy electron diffraction (SPA-LEED) image. Besides the known SiC and graphene diffraction patterns and the quasi- $(6 \times 6)$  reconstruction, Pb-induced diffraction spots (marked with red arrows) around the (00) and all first order spots are clearly visible. The Pb-induced structures are formed along the zigzag direction of the graphene and can be interpreted as a quasi  $(10 \times 10)$  reconstruction with respect to graphene and correlate nicely with the distance of 2.3 nm in between the centers of the hexagons. Moreover, higher order diffraction spots of Pb-induced structures can be resolved at low temperatures as shown by the zoom into the area around the (00) spot in panel (c). Compared to the  $(6 \times 6)$  spots, reflecting the symmetry of the graphene layer with respect to the SiC(0001) surface, the Pb-induced spots are broadened, something which is seen in former studies as well.<sup>[24,25]</sup> In addition, as shown in **Figure 1d**, the Pb-induced diffraction spots, e.g.,  $Pb_{rec}(10)$  and  $Pb_{rec}(11)$ , are azimuthally elongated and can be fitted best by assuming two peaks with the same half-widths, which is expected for the model, we provide below.

For developing this model it is of crucial importance to know the thickness of the intercalated layer. In order to prove the successful intercalation of a Pb ML, we investigated the vertical geometry of the heterostructure using normal incidence x-ray standing wave (NIXSW). In **Figure 2a–c**, we show typical x-ray photoelectron (XP) spectra of the Pb 4f<sub>7/2</sub>, Si 2s, and C 1s core levels, respectively. They were recorded using hard x-rays at a photon energy close to the Bragg energy of the SiC(0006) reflection

B. Matta, P. Rosenzweig, K. Küster, U. Starke  
Max-Planck-Institut für Festkörperforschung  
Heisenbergstr. 1, 70569 Stuttgart, Germany  
C. Polley  
MAX IV Laboratory  
Lund University  
Fotogatan 2, 22484 Lund, Sweden

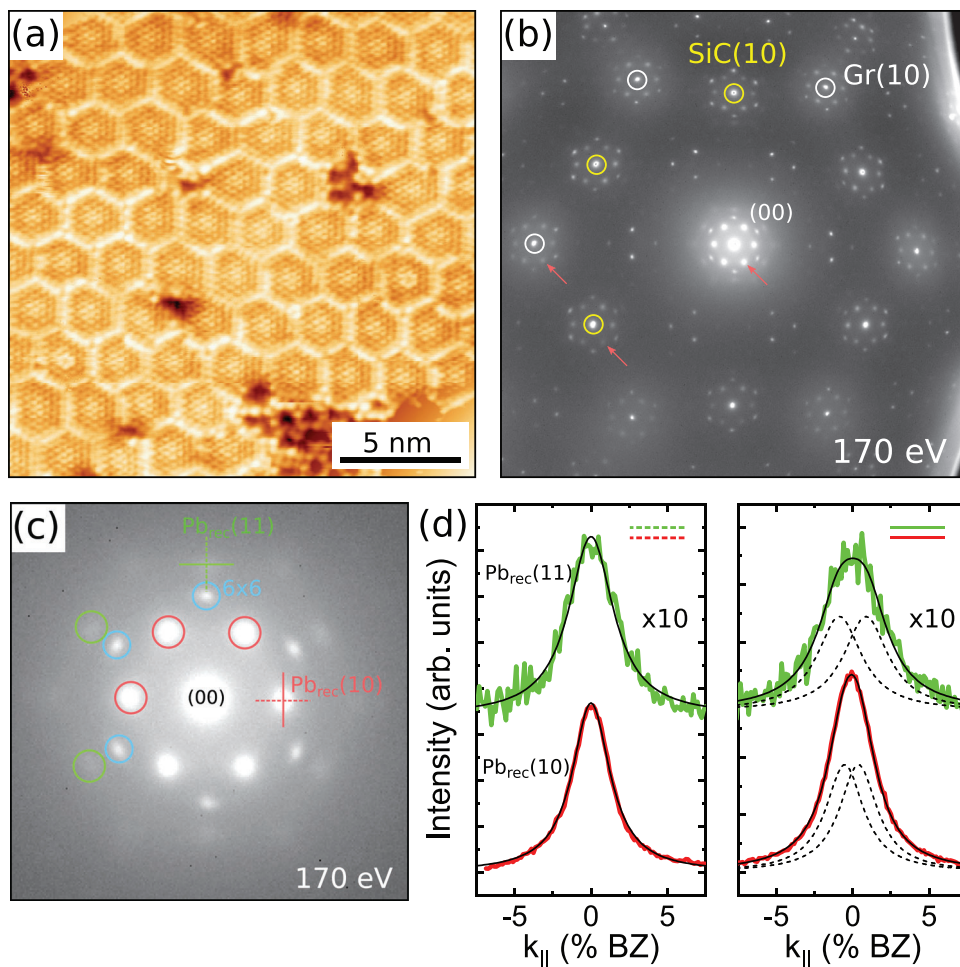


**Figure 1.** a) Overview STM image ( $20 \times 20 \text{ nm}^2$ ,  $U_{\text{bias}} = +1 \text{ V}$ ,  $I = 0.1 \text{ nA}$ ). b) SPA-LEED image taken at 170 eV and 80 K. Integer spots of the SiC and graphene lattice are marked by circles. Red arrows indicate the Pb-induced diffraction spots. Besides the integer diffraction spots also diffraction spots of the  $(6\sqrt{3} \times 6\sqrt{3})$  lattice are visible. c) Magnified (00)-spot area revealing also higher-order diffraction spots of the superstructure induced by intercalated Pb. d) Radial (left) and azimuthal (right) line scans (after subtraction of the bell-shaped background) across different reconstruction spots as indicated in (c). The Pb-induced diffraction spots, e.g.,  $\text{Pb}_{\text{rec}}(10)$  and  $\text{Pb}_{\text{rec}}(11)$ , reveal a strong azimuthal broadening, which is fitted by two peaks. The half-width was taken from the radial scans.

in back-diffraction geometry. Figure 2d shows the corresponding photoelectron yield curves with best fits, from which we determined the coherent positions and fractions, as well as a typical reflectivity of the Bragg reflection. Appropriate corrections for non-dipolar effects were considered where possible, that is for the  $s$ -states C 1s and Si 2s.<sup>[38]</sup>

The results are plotted in the Argand diagram shown in Figure 3a. In this polar diagram, every data point represents the head of a polar arrow, which in turn represents the coherent fraction (length of the vector) and position (polar angle) obtained from fitting the corresponding yield curve. For all atomic species, the individual data points, recorded at different positions on the sample within an area of more than  $6 \text{ mm}^2$ , show a very small variation, indicating a very homogeneous sample. In Table 1, the average values for the coherent position and fraction, and the corresponding heights with respect to the surface are given.

As reference, the data of a BL/SiC(0001) are shown in Figure 3a (red data points ( $C_{\text{BL}}^{\text{PASG}}$ )). This sample was prepared using the

PASG method as described in Ref. [39]. Both, coherent position and fraction of this sample, agree nicely with previous results for samples prepared in an Ar atmosphere without polymer (SG).<sup>[40,41]</sup> We therefore conclude that the preparation method (PASG or SG) has no significant influence on the vertical structure of the BL.

Compared to these reference data for the BL, the coherent position of graphene in the Pb-intercalated sample differs clearly (purple ( $C_{\text{G}}$ ) data points in Figure 3a, and Table 1), which confirms the change of the vertical position of the graphene layer due to intercalation. The corresponding height-model is depicted in Figure 3b. The coherent fraction of Pb  $4f_{7/2}$  is close to unity, thus indicating that the Pb-atoms are located at the same height with respect to the nearest Bragg plane. This means that for the case of more than one Pb layer being present in the sample, the distance between these layers must be very close to the Bragg plane spacing  $d_{0006}^{\text{SiC}} = 2.52 \text{ \AA}$  (or a multiple of this value), since otherwise the coherent fraction would be significantly reduced.

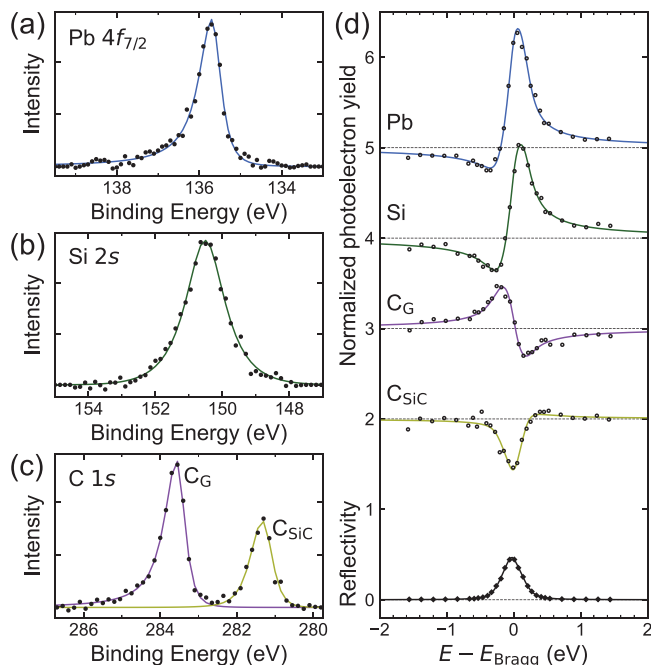


**Figure 2.** a–c) XPS spectra of Pb  $4f_{7/2}$ , Si  $2s$  and C  $1s$  measured at an x-ray energy of 2459.8 eV (1.5 eV above the energy of the (0006) Bragg reflection) and the corresponding best fits.  $C_G$  and  $C_{SiC}$  represent the emission from carbon atoms in graphene and SiC, respectively. A Shirley background was subtracted. d) Photoelectron yield curves for the different core levels and the reflectivity of the (0006) Bragg reflection. For clarity, the yield curves of  $C_{SiC}$ ,  $C_G$ , Si, and Pb are shifted vertically by 2, 3, 4, and 5, respectively.

**Table 1.** Averaged values for the coherent position  $P_c^H$  and fraction  $F_c^H$ , as obtained from several (up to 11) individual NIXSW measurements on Pb-intercalated graphene and, as a reference, of the non-intercalated graphene BL on SiC(0001). The height  $z$  w.r.t. the surface is calculated by  $z = d_{0006}^{SiC} (n + P_c^H - P_{c-Si}^H)$ , where  $n$  is the number of Bragg planes between the considered atomic species and the surface, and  $d_{0006}^{SiC} = 2.52$  Å is the lattice spacing of the reflection used. Parameters used in the fitting procedure: Deviation from perfect normal incidence  $\xi = 3.5^\circ$ , averaged electron emission angle relative to the incident synchrotron beam  $\phi = 80.9^\circ$ , non-dipolar correction factors (only applicable for s-state emission)  $\gamma_{C\ 1s} = 1.022$ ,  $\Delta_{C\ 1s} = -0.218$ ,  $\gamma_{Si\ 2s} = 0.707$ , and  $\Delta_{Si\ 2s} = 2.645$ . For details of the analysis procedure see Ref. [38].

	$P_c^H$	$F_c^H$	$n$	$z$ (Å)
$C_G\ 1s$	0.548(8)	0.69(8)	2	6.39(3)
Pb $4f_{7/2}$	0.09(2)	1.05(6)	1	2.72(3)
Si $2s$	0.013(3)	1.00(2)	0	0.00
$C_{SiC}\ 1s$	0.763(8)	0.94(3)	−1	−0.63(2)
$C_{BL}^{PASG}\ 1s$	0.925(3)	0.76(2)	0	2.34(1)
$C_{BL}^{SG}\ 1s^{[41]}$	0.945(3)	0.77(4)	0	2.30(2)

However, if we had multiple intercalated layers, the distance between these layers would be significantly larger than 2.52 Å. A value of 2.86 Å would be a lower limit for this distance. It corresponds to the interlayer distance between close-packed Pb layers in a fcc bulk crystal. But since the Pb layer in our case is laterally compressed, the vertical spacing would be significantly larger than 2.86 Å. Seehofer et al. reported a compression of 3–5% for

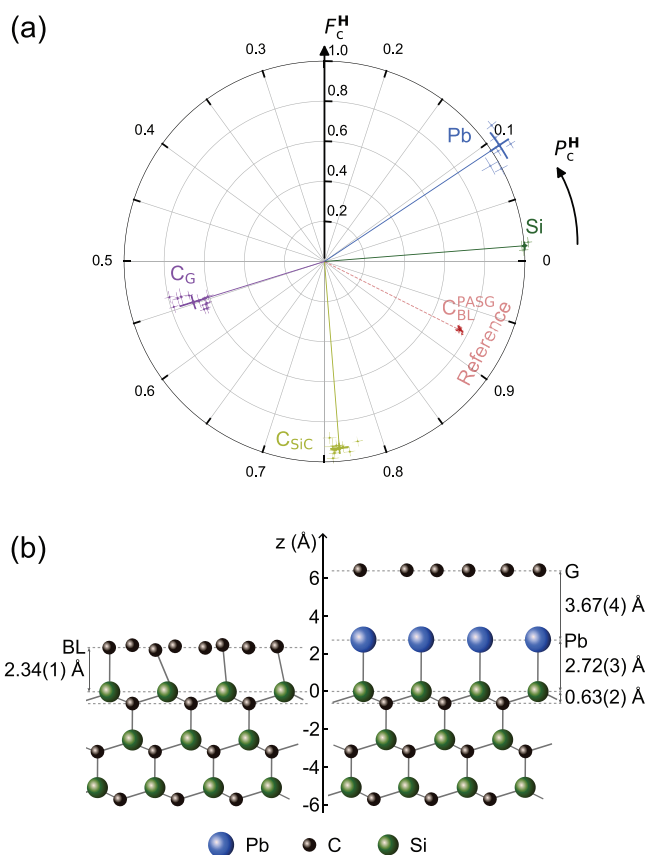


**Figure 3.** a) Argand diagram showing all individual results of the NIXSW analysis for the Pb-intercalated graphene on SiC(0001) sample (blue, purple, and dark and light green) and the non-intercalated BL structure as reference (red, BL species only, no bulk species shown). Each data point is shown with its individual error in  $P_c^H$  and  $F_c^H$ . The lines and the thicker error bars indicate the average values. b) Simplified ball-and-stick model of the vertical structure of the BL (left) and Pb-intercalated graphene on SiC(0001) (right) neglecting details of the grain boundary structure (cf. Figure 4a).

the different ( $\sqrt{3} \times \sqrt{3}$ ) Pb phases on Si(111),<sup>[32]</sup> which we use as the starting model for the intercalated Pb layer. Based on a 3% lateral compression and conservation of the volume of Pb, a rough estimate for the expansion of the layer spacing would be 6.3%, which in turn corresponds to a Pb interlayer spacing of more than 3 Å. A bilayer with such a large lattice spacing would significantly reduce the measured coherent fraction for Pb. Already for an uncompressed close-packed Pb bilayer one expects a reduction of the coherent fraction  $F_c^H$  by about 10%. For the more realistic scenario of a 3% laterally compressed bilayer, the expected decrease would be more than 20%, which is certainly not compatible with our experimental result. This allows us to conclude from the NIXSW data, that there are (regarding their size) no significant bi- or even multi-layer domains present in our sample.

Figure 3b depicts the vertical structures of the BL and the Pb-intercalated graphene on SiC(0001). The measured Si-Pb distance  $\Delta z_{Si-Pb} = 2.72(3)$  Å is close to the expected covalent bonding distance of 2.60 Å,<sup>[42]</sup> suggesting a chemical bond between



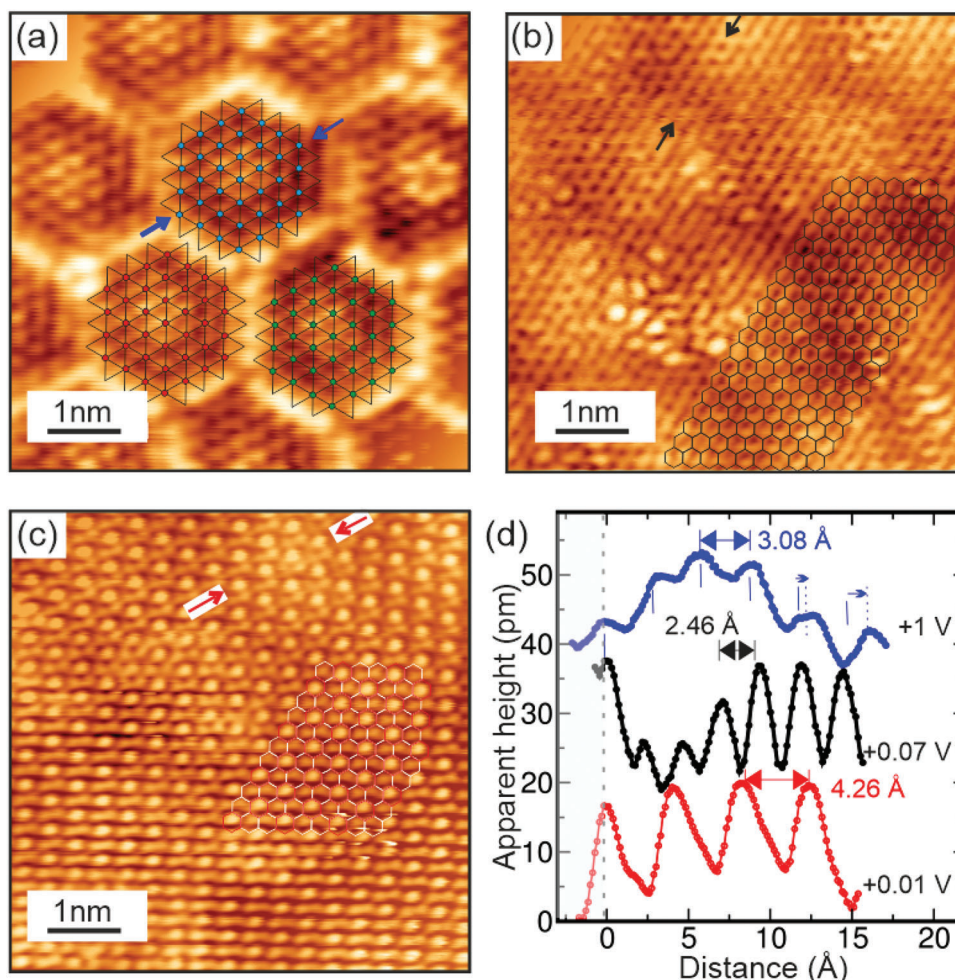


**Figure 4.** a–c) Zoomed-in STM images ( $6 \times 6 \text{ nm}^2$ ) of the same area taken under different tunneling conditions ( $U_{\text{bias}} = +1 \text{ V}$ ,  $+0.07 \text{ V}$ , and  $+0.01 \text{ V}$ , respectively,  $I = 0.1 \text{ nA}$ ). The overlaid  $\text{SiC}(1 \times 1)$  model in (a) shows that the atoms in between adjacent hexagons are shifted with respect to each other. The graphene lattice (b) and the  $(\sqrt{3} \times \sqrt{3})$  reconstruction w.r.t graphene (c) become visible at bias voltages close to Fermi energy and are long-range ordered across the Pb-structure underneath. d) Line scans (shifted) taken along the directions indicated by the arrows in (a–c).

Pb and Si that saturates the dangling bonds of the Si surface atoms. On the other hand, the measured separation between Pb and graphene of  $3.67(4) \text{ \AA}$  even exceeds slightly the sum of the van der Waals radii of Pb and C of  $3.55 \text{ \AA}$ ,<sup>[43]</sup> indicating a very weak interaction. We conclude that the Pb layer efficiently decouples the graphene layer from the substrate in full agreement with our STM, X-Ray Photoelectron Spectroscopy (XPS), and angle-resolved photoelectron spectroscopy (ARPES) results (see below).

Further details of the Pb-induced interface structure become visible in STM under different tunneling conditions. In **Figure 4a** the periodicity seen in the central part of each of the hexagons at a bias voltage  $U_{\text{bias}}$  of  $+1 \text{ V}$  is close to the lattice constant of SiC,  $a_{\text{SiC}} = 3.08 \text{ \AA}$ . As obvious from the (blue) line scan shown in **Figure 4d**, the positions in the vicinity of the center appear a little shifted. The fact, that the central atoms appear higher compared to those in the vicinity points toward slightly different adsorption sites within the SiC UC. Interestingly, the atomic lattices of adja-

cent hexagons are shifted with respect to each other. This comes directly along with the strain-induced formation of grain boundaries in between the hexagons.

The atomic structure of graphene is resolved with lower bias voltages, **Figure 4b**. The graphene lattice extends continuously over the buried grain boundary structure and therefore also allows the lattice constants of the Pb layer and the orientation of the Pb reconstruction to be determined in combination with panel (a). At even lower tunneling voltages,  $U_{\text{bias}} = +10 \text{ meV}$ , a long-range ordered,  $(\sqrt{3} \times \sqrt{3})$ -reconstructed pattern with respect to graphene is found (cf. **Figure 4c**). The corresponding line scans, shown in **Figure 4d**, reproduce nicely the lattice constants of graphene and the  $(\sqrt{3} \times \sqrt{3})$  reconstruction. This reconstruction, which we have seen in STM but not in LEED (cf. **Figure 1b**), is compatible with a Kekulé ground state of graphene.<sup>[44]</sup> Further details will be discussed below.

For all bias voltages, the STM patterns can be explained by the three above mentioned motifs. This is in contrast with our

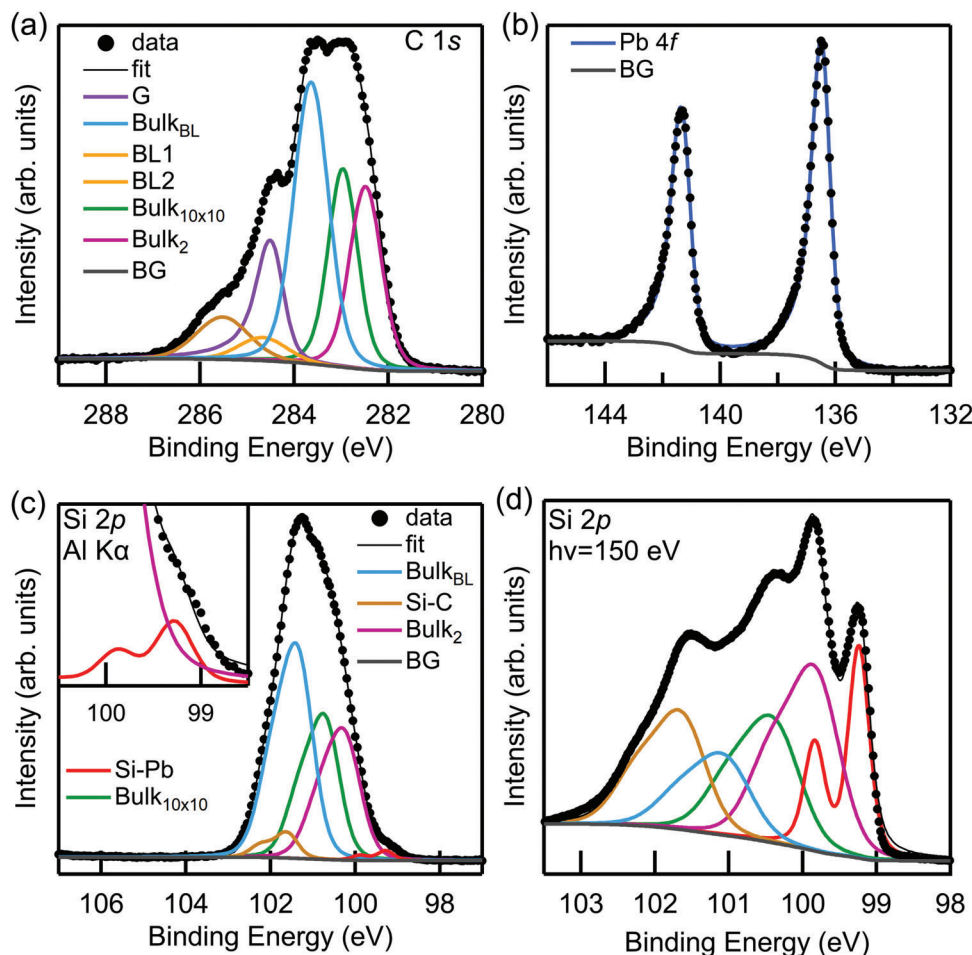


**Figure 5.** a) The C 1s spectrum exhibits a strong graphene (G) component together with contributions from the decoupled substrate ( $\text{Bulk}_{10 \times 10}$ ,  $\text{Bulk}_2$ ) and remnants of pristine BL ( $\text{Bulk}_{\text{BL}}$ , BL1, BL2). A Shirley background (BG) has been applied to all core-level spectra. b) The Pb 4f core-level shows a single, asymmetric component. c) The Si 2p data show the components associated with the decoupled bulk (see (a)) as well as the bulk and surface component associated with the BL ( $\text{Bulk}_{\text{BL}}$ , Si-C) and in addition a surface component Si-Pb of substrate atoms bond to the intercalant layer (inset). d) The surface sensitive measurement of the Si 2p core-level emphasizes the surface components and reveals the narrow character of the Si-Pb component. The labeling of components is according to (c).

recent paper, where we analyzed intercalated Pb stripes and where the more complex STM Moiré features could be explained only assuming at least two intercalated Pb layers.<sup>[26]</sup> Thus, in agreement with NIXSW, STM confirms here also the successful intercalation of a single Pb ML interface structure in the present case. Moreover, we can exclude that the Pb-induced reconstruction spots are due to a Moiré. Instead, they emerge due to a strain-induced grain boundary structure at the interface. The apparent height of the grain boundaries does not exceed 25 pm. As will be shown in Figure 7, the concentration of the grain boundary sites is around 20%. Owing to this small concentration and small buckling, a significant effect on the Pb coherent fraction is not to be expected.

## 2.2. Electronic Structure

Photoelectron spectroscopy is used to verify the decoupling of the BL in the intercalation process and to determine the chemical environment at the surface. Figure 5a shows a C 1s core-level

obtained after the Pb intercalation with a strong graphene component (G) at 284.4 eV indicating the partial transformation of BL regions into almost charge-neutral freestanding MLG.<sup>[45]</sup> This comes along with the formation of bulk contributions  $\text{Bulk}_{10 \times 10}$  and  $\text{Bulk}_2$  at 282.96 and 282.48 eV, respectively, which are shifted by 0.68 and 1.16 eV with respect to the non-intercalated bulk bond to BL at 283.64 eV ( $\text{Bulk}_{\text{BL}}$ , light blue).<sup>[45]</sup> The shift is due to an upward band bending associated with the modified bonding characteristics in the intercalated surface region, where the Si dangling bonds are now well saturated by Pb. Note that the occurrence of two well-separated intercalated bulk peaks points toward the formation of at least two different intercalation phases, which is not surprising given the rich phase diagram of Pb on, e.g., Si surfaces.<sup>[35]</sup> The bulk component labeled  $\text{Bulk}_{10 \times 10}$  was already observed in earlier studies<sup>[25]</sup> and can be associated with the hexagonal (mottled) phase giving rise to the  $(10 \times 10)$  superperiodicity discussed in this study. The nature of the second intercalated phase is as of yet unknown and needs further investigation. In addition, the components BL1 and BL2 belong to  $\text{sp}^3$ - and  $\text{sp}^2$ -hybridized carbon atoms in the BL on

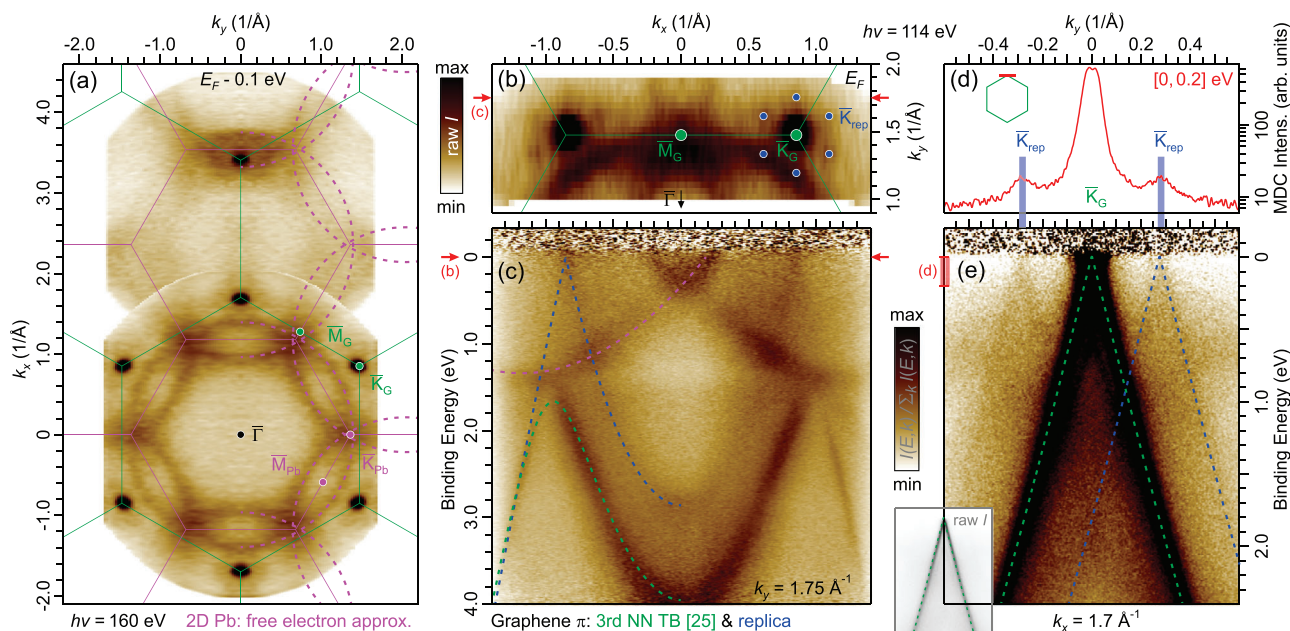


**Figure 6.** a) ARPES constant energy surface of Pb-intercalated quasi-freestanding graphene combined from two polar deflection maps at normal emission and 26° tilt. The 2D interlayer bands of Pb are overlaid by the circular contours of a free electron model (dashed pink curves) sharing a  $(1 \times 1)$  periodicity with respect to the SiC surface. Green and pink hexagons indicate the first and repeated BZs of graphene and SiC  $(1 \times 1)$ , respectively. b) Fermi surface revealing replicated graphene  $\pi$ -bands (blue discs,  $\bar{K}_{\text{rep}}$ ) around the main  $\bar{K}_G$  points. c) Corresponding dispersion profile  $E(k_x)$  between the red arrows in (b) at  $k_y = 1.75 \text{ \AA}^{-1}$ , cutting through the  $\pi$ -bands at the outermost  $\bar{K}_{\text{rep}}$  point, with the tight-binding (TB) fit from Ref. [25] overlaid on the replicated (blue curve) and main  $\pi$ -band (green curve) and the free electron model tracing the Pb band (purple curve). d) MDC through  $\bar{K}_G$  perpendicular to  $\bar{K}_G$  elucidating the replicated  $\bar{K}_{\text{rep}}$  points. Blue bars indicate a range from  $0.268$  to  $0.294 \text{ \AA}^{-1}$  for the superstructure momentum vector covering the span between  $(11 \times 11)$  and  $(10 \times 10)$ . e) Dispersion profile  $E(k_y)$  parental to (d), with main and replica cones overlaid by the TB fit from Ref. [25] (green and blue lines, respectively). c,e) Intensity normalized to  $k$ -integrated intensity. Inset in (e): raw data.

top of the non-intercalated bulk areas. From the intensity ratio  $\text{Bulk}_{\text{BL}}/(\text{Bulk}_{\text{BL}} + \text{Bulk}_{10 \times 10} + \text{Bulk}_2) = 0.45$ , we find that 55% of the investigated surface area are intercalated and the ratio of the bulk peaks  $\text{Bulk}_{\text{BL}} : \text{Bulk}_{10 \times 10} : \text{Bulk}_2$  equals to 45.3% : 27.4% : 27.3%.

The Pb 4f core-level in Figure 5b is readily described with a single, asymmetric Mahan-lineshape<sup>[46]</sup> doublet with the  $4f_{7/2}$  peak at 136.5 eV and a spin-orbit splitting of 4.87 eV in full consistency with existing literature values for intercalated Pb.<sup>[25]</sup> The lineshape is an unambiguous manifestation of the metallic character of the 2D Pb layer, in agreement with measurements of the Fermi surface of this phase<sup>[25]</sup> (cf. also Figure 6). Since there is no additional peak found associated with bulk Pb, we conclude that no excess Pb resides on the surface. From the intensity of the Pb 4f line compared to the bulk C 1s (Si 2p) components, and taking into account an atom density of  $1.2 \times 10^{15} \text{ C (Si) atoms per cm}^2$  in the substrate<sup>[47]</sup> and  $1.0 \times 10^{15} \text{ Pb atoms per cm}^2$  in the Pb layer, respectively, we determine an average Pb thickness of  $(1.5 \pm 0.5) \text{ \AA}$ . This is compatible with the monolayer model obtained from the NIXSW data.

The Si 2p core-level in panel (c) can be decomposed into five distinct spin-orbit split doublets: two surface components at 101.62 eV (Si-C, yellow) and 99.28 eV (Si-Pb, red) associated with Si atoms bonded to C atoms of the BL and Pb atoms,<sup>[48]</sup> respectively, and three bulk components at 101.33 eV ( $\text{Bulk}_{\text{BL}}$ , light blue), 100.67 eV ( $\text{Bulk}_{10 \times 10}$ , green) and 100.23 eV ( $\text{Bulk}_2$ , purple). The surface component associated with the intercalated regions

Si-Pb exhibits a rather small Gaussian width that is only half the value of the Si 2p bulk components. This most likely results from a better screening of the core-hole due to the bonding to the metallic Pb. A similar observation has been made for partially oxidized TiSi<sub>2</sub>, where the Si-Ti component is significantly sharper than the corresponding Si-O component<sup>[49]</sup> as well as for metallic Si nanowires on Ag(110) with a lineshape being even narrower than for a bulk Si crystal.<sup>[50]</sup> This behavior gets even more obvious from the surface sensitive measurement ( $h\nu = 150 \text{ eV}$ ) in panel (d), where the intensity of the surface components is strongly enhanced compared to the bulk components. Please note, that the measurement in (d) was obtained from an independently prepared sample and thus shows a different ratio of the bulk components.

The bulk components of the intercalated areas in (c) are shifted by 0.66 eV and 1.1 eV with respect to the non-intercalated bulk, and thus, closely resemble the band bending obtained from the C 1s core-level in (a). The intensity ratio of the three bulk components  $\text{Bulk}_{\text{BL}} : \text{Bulk}_{10 \times 10} : \text{Bulk}_2$  equals to 43.8% : 28.8% : 27.4%, which agrees well with the ratios measured from the C 1s spectrum. Furthermore, the difference in the binding energy for the two intercalated phases obtained from the spectrum in (d) amounts to 0.54 eV and agrees nicely with the less surface sensitive data in (a) and (c). The overall agreement of core-level shifts and intensity ratios for the bulk components corroborates our model of coexisting intercalation phases. Please note, that the sample described in Figures 2 and 3 showed a slightly larger



degree of intercalation of 85% and an intensity ratio for the intercalated bulk components of  $\text{Bulk}_{10 \times 10} : \text{Bulk}_2 = 20\%$ . However, since we find the coexistence of mixed intercalation phases in both cases, it is valid to compare the complementary results with each other. Nevertheless, the nature of the mixed phases holds open questions for future studies.

The band structure of both the quasi-freestanding graphene after Pb-intercalation and the emerging Pb interface layer were investigated by synchrotron-based ARPES measurements. From the band structure of the Pb interface, we can conclude that the Pb layer has a principle arrangement in line with the SiC periodicity: In Figure 6a a constant energy surface (CES) at 0.1 eV (integrated over  $\pm 50$  meV) below the Fermi level  $E_F$ , acquired using a photon energy of  $h\nu = 160$  eV, shows - in addition to the graphene bands already converging towards their charge neutrality point - nearly circular features representing the Pb bands. In a first approximation they can be fitted by a free electron model. These giant circular contours repeat with a periodicity that corresponds to the  $(1 \times 1)$  periodicity of the SiC surface. The CES rendition is combined from two deflection maps, one at normal emission and one at  $26^\circ$  tilt in the  $\overline{\Gamma K}$  direction of graphene, and reveals the first and the repeated Brillouin zones (BZs) of the Pb interface being identical to those of the SiC substrate.

Also the quasi  $(10 \times 10)$  superstructure can be monitored in ARPES. The Fermi surface shown in Figure 6b reveals additional spectral features in the vicinity of the main  $\overline{K}_C$  points, so-called replica cones ( $\overline{K}_{\text{rep}}$ ). These replica features are most prominently visible at a photon energy of  $h\nu = 114$  eV, which was therefore used to record also the dataset of Figure 6d,e. The distance of these  $\overline{K}_{\text{rep}}$  points corresponds to about the momentum vector  $k_{\text{rep}}$  of the superstructure. A quantitative evaluation can be retrieved by fitting the bands visible in an  $E(k_x)$  dispersion profile (Figure 6c) measured through such a replica cone (position indicated in panel (b) by red arrows). The replica cone is perfectly simulated by the 3rd nearest-neighbor tight-binding model (NN-TB) from Ref. [25]. The replica momentum vector is determined by correlating the band bottom of the main graphene  $\pi$ -band (green curve) to the correspondingly shifted TB model as well as by adjusting the quasi-free electron model of the Pb band (purple curve).

This yields  $k_{\text{rep}} \approx 0.28 \text{ \AA}^{-1}$ , which would correspond to a superstructure unit vector slightly larger than ten times the graphene UC. In the high resolution  $E(k_y)$  dispersion through the  $\overline{K}_C$  point (acquired perpendicular to the  $\overline{\Gamma K}$  direction of graphene's BZ) shown in Figure 6e the replica cones are clearly visible, and they also fit well the 3rd NN-TB model. The momentum position of the replicas can be evaluated from a momentum distribution curve (MDC) (Figure 6d) obtained from the dispersion map in panel (e) by integrating single MDCs from  $E_F$  to 200 meV binding energy. Within the experimental uncertainty of the broad peaks,  $k_{\text{rep}}$  appears to be located within the momentum range indicated by the blue bars that correspond to a periodicity span from  $(10 \times 10)$  to  $(11 \times 11)$ . Note that in panels (c) and (e) of Figure 6 the intensity  $I(E, k)$  has been divided by the  $k$ -integrated intensity  $\Sigma_k I(E, k)$  to enhance the visibility of the replicated  $\pi$ -bands. Panels (a) and (b) show raw intensities symmetrized over graphene's  $\overline{K\Gamma K}$  ( $k_y = 0$ ) and  $\overline{M\Gamma M}$  ( $k_x = 0$ ) lines, respectively. With the fit of the

band course in panel (c) and the location of the  $\overline{K}_{\text{rep}}$  points on the momentum scale (panel d), ARPES corroborates the periodicity assessment of the Pb reconstruction from STM and SPA-LEED and is even consistent with the spot broadening away from a strict  $(10 \times 10)$  superperiodicity. Note, that for the measurements shown in panels (a–c) and (d,e) different samples with slightly different Pb intercalation recipes were used, proving the robustness of the intercalation procedure.

The linear dispersion of the graphene  $\pi$ -bands clearly demonstrates the formation of freestanding graphene in agreement with our NIXSW results. Thereby, for different measurements using different samples and different experimental setups (synchrotron, conventional home-lab ARPES, momentum microscopy) the Dirac crossing energy  $E_D$  consistently lies just slightly above the Fermi energy in a regime of  $E_D - E_F \approx 4$ –15 meV, which demonstrates almost perfectly charge-neutral graphene with a residual hole concentration of less than  $p = 1.8 \times 10^{10} \text{ cm}^{-2}$ . From this observation, we can construct two possible doping scenarios: i) the Pb atoms saturate the dangling bonds of the topmost Si atoms, which are otherwise known to transfer around  $n = 1.2 \times 10^{13} \text{ cm}^{-2}$  electrons to the graphene layer in case of epitaxial MLG<sup>[51]</sup> and at the same time the metallic Pb layer at least partially screens the graphene from the spontaneous polarization of the substrate leading to the pronounced p-type doping for, e.g., H-intercalated graphene,<sup>[51,52]</sup> or ii) the charge transfer and the spontaneous polarization of the substrate are coincidentally compensated by charge transfer from the Pb itself.

### 2.3. Model for the Intercalated Pb Monolayer Phase

In order to derive a reasonable model, we start our discussion with the well-investigated Pb/Si(111) system.<sup>[19,35,53]</sup> Of particular interest is the  $\alpha$ -Pb phase, which represents a highly compressed state of a densely packed Pb ML. In Figure 7a we show the  $\alpha$ -Pb phase on Si(111) forming a  $(\sqrt{3} \times \sqrt{3})$  structure with four Pb atoms in the UC referring to  $1.0 \times 10^{15} \text{ Pb atoms per cm}^2$ . Figure 7a also shows the same Pb UC, but now superimposed onto the SiC(0001) lattice. As obvious, the  $\alpha$ -Pb phase structure fits almost perfectly on the SiC( $1 \times 1$ ) UC in agreement with our STM findings (cf. Figure 4a).

The periodic extension of this UC over the SiC(0001) lattice is shown in Figure 7b. The Moiré reveals a periodicity, which is close to the one shown in Figure 1a. Similar models were suggested before.<sup>[20,25]</sup> However, the structure cannot resemble the abrupt contrast change seen in our STM experiments upon changing the bias voltages.

A model that accounts for all above mentioned details is suggested in Figure 7d. Here the basic building block is a hexagonal Pb supercell that contains 12  $\alpha$ -Pb UCs, i.e., 48 Pb atoms (cf. Figure 7c). In order to account for the misfit between the  $\alpha$ -Pb UC and SiC(0001), the building blocks need to be shifted by a SiC lattice vector, e.g., seen in Figure 4a. Along with this, grain boundaries are necessarily formed.

For the case shown in Figure 7d, each building block was shifted by the same vector (black arrows). Depending on the details of nucleation, the displacement can occur along different SiC directions, which explains the defects of the quasi-hexagons and their edges observed in our experiments. The positioning of



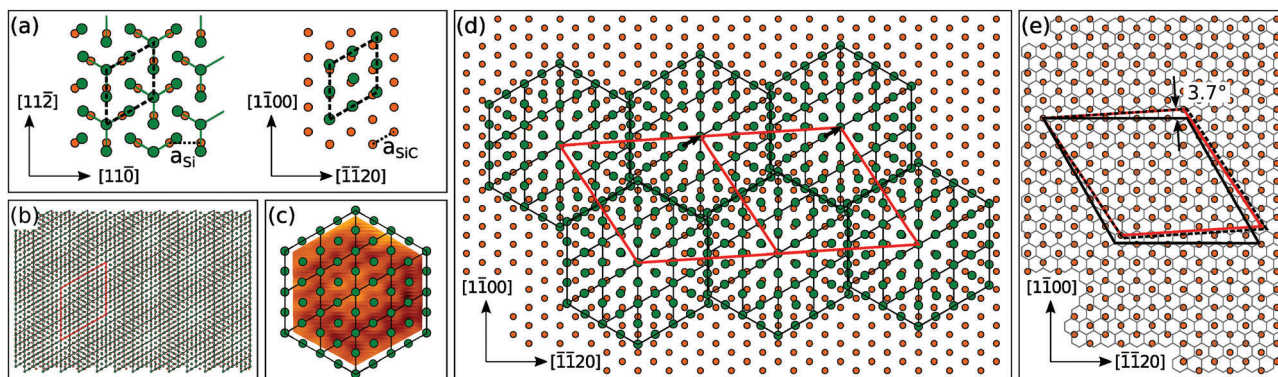


**Figure 7.** a) Ball-and-stick models of  $\alpha$ -Pb on  $H_3$  positions on Si(111) (left) and  $T_4$  positions on SiC(0001). The green and orange circles denote Pb atoms and the topmost Si layer, respectively. b) Periodic continuation of  $\alpha$ -Pb on SiC(0001) showing a Moiré pattern. c) The hexagonal building block consists of 12  $\alpha$ -Pb units, i.e., 48 Pb atoms, superimposed to an STM image. d) Grain boundary model where the building blocks are shifted by a SiC lattice vector w.r.t. each other (black arrows). Possible relaxation effects within the Pb ML are neglected in this model. e) The (red) rhombus shows the UC of the complete Pb ML and resembles a quasi ten-fold periodicity w.r.t. graphene (black rhombus), which is rotated by  $3.7^\circ$ . The Pb atoms are omitted for clarity.

the supercells on  $T_4$  positions on SiC(0001) also reflects very well the central structure of the hexagons. The neighboring atoms around the central one also occupy on-top positions giving rise to a different contrast compared to the outer areas of the hexagons (cf. line scan in Figure 4d). Please note, the model shown in panel (d) is built from the unrelaxed  $\alpha$ -Pb structure. Given the line scans discussed in connection with Figure 4d, the Pb atoms and thus the grain boundaries most likely relax a little further, which is not accounted for in the model.

The UC of the quasi-hexagonal structure is rotated by  $3.7^\circ$  w.r.t. the  $\langle 11\bar{2}0 \rangle$  direction and contains 61 Si atoms. It should be pointed out that this UC is close to the one suggested by Ref. [25], plotted as black rhombus in Figure 7e. While this Moiré pattern is commensurate with graphene, we propose here a model providing a strict commensurability with respect to SiC. Assuming, that long-range ordered domains with this quasi ten-fold periodicity w.r.t. graphene are formed, different domains should cause a splitting of the Pb-induced reconstruction spots. The analysis of the azimuthal spot broadening of the Pb-induced reconstruction spots in Figure 1d refers to an angle of around  $2.5^\circ$  w.r.t. the  $\langle 11\bar{2}0 \rangle$  direction in reasonable agreement with the above mentioned value.

Most interestingly, the UC of the quasi-hexagonal structure and the grain boundaries comprises also 61 Pb atoms, which allows for a perfect saturation of all Si-dangling bonds giving rise to a charge-neutral graphene in agreement with our ARPES analysis and recent studies.<sup>[24,25]</sup>

The grain boundary model shown in Figure 7d suggests a formation of dimer-like grain boundary edges and trimer-like corners. Some of these structural features are visible in Figure 1a. In order to get more insight into the details, we performed first scanning tunneling spectroscopy (STS) measurements shown in Figure 8. A characteristic peak at around -200 meV is visible, most likely related to the Pb-induced mini-parabola seen in ARPES, cf. Figure 6c). The peak position and splitting depend sensitively on the tip position within the  $\alpha$ -Pb UC, thus most likely sampling Pb states. This interpretation is in agreement with previous STS measurements on intercalated Pb multilayer structures.<sup>[26]</sup> A sharp single peak is found for the occupied states in the cen-

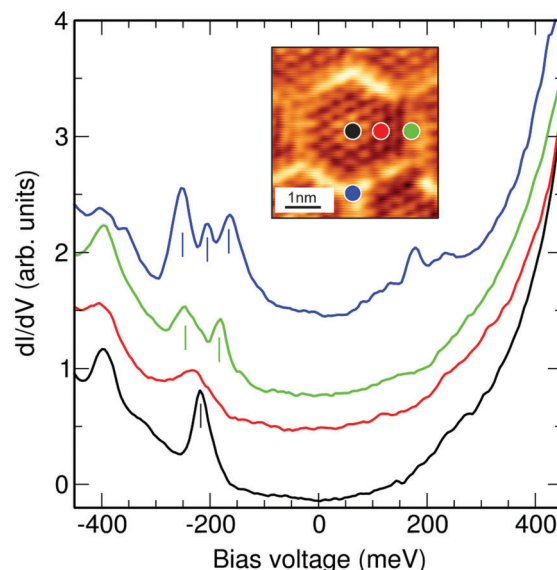


**Figure 8.** STS spectra at various sites of the supercell, as indicated in the inset. The spectra shown represent averaged values over three equivalent positions each. The peak at around -200 meV resembles a Pb-state and shows characteristic dimerization and trimerization if spectra taken at the boundary and corners, respectively.

ter of the hexagon and becomes broadened when moving toward the rim of the hexagon. Thereby, this peak splits into two peaks when the tip is positioned on the edge, while three peaks are found at the corner sites. According to the ball-and-stick model (cf. Figure 7d) at these sites, two and three Pb atoms are close by, which is represented by a hybridization.

### 3. Conclusion

To conclude, we presented a detailed study for a Pb ML reconstruction obtained upon Pb-intercalation at the interface of epitaxial graphene on SiC. The Pb-induced quasi ten-fold periodicity seen in various experiments is rather a grain boundary

effect and triggered by the compressive strain. The formation of heavy-wall domain grain boundaries comes along with a rotation of the Pb-induced supercell as analyzed in detail by STM and STS. Moreover, in presence of domain walls, the number of Pb atoms nicely match the number of Si adatoms and allows for a perfect compensation of surface dangling bonds giving rise to quasi-charge-neutral graphene. This effective decoupling mechanism is in full agreement with our results obtained from ARPES and NIXSW measurements.

To the best of our knowledge, the intercalation of Pb has made it possible to produce the most charge-neutral epitaxial graphene to date. Although hydrogen allows a much simpler and more efficient saturation of the Si-dangling bonds, it is shown that already a single layer of Pb can efficiently shield or compensate the spontaneous polarization of the SiC surface.<sup>[51]</sup>

Regarding the  $(\sqrt{3} \times \sqrt{3})$  phase in graphene, we cannot provide a complete picture at this point. However, it is striking that we have found this reconstruction so far only in STM at very low tunneling voltages. From the fact that this reconstruction forms even without adsorbates, e.g., as seen for Li adatoms,<sup>[44]</sup> the following conclusions can be drawn for the moment: the domain boundaries of the Pb interlayer seem to act as scatterers for the  $\pi$ -electrons of graphene and allow the formation of a long-range ordered Kekulé phase. The nesting condition for this phase is almost perfectly satisfied due to the charge neutrality in the graphene. However, we did not observe signs of the Kekulé phase in the LEED ( $\approx 80$  K) and ARPES ( $\approx 20$  K) investigations, which were carried out at higher temperature compared to the LT-STM (4 K) experiments. We therefore cannot rule out temperature effects at least partially destroying the Kekulé phase.

As mentioned above, superconductivity has already been demonstrated for similar structures of a Pb ML on Si(111).<sup>[29]</sup> Future measurements will show whether this intercalated 2D Pb layer on SiC also becomes superconducting or even induces superconductivity in graphene.

## 4. Experimental Section

**Sample Preparation:** As substrate for graphene synthesis, nominally on-axis, n-type 6H-SiC(0001) (PAM-Xiamen Co., Ltd.), 4H-SiC(0001) (Cree, Inc.) or 6H-SiC(0001) (SiCrystal GmbH) wafers were used. The wafers were wet-chemically cleaned according to Ref. [54] and BL growth was carried out in an inductively heated hot-wall reactor<sup>[55]</sup> utilizing the polymer assisted sublimation growth (PASG) proposed by Kruskopf et al.<sup>[39]</sup> Here, the photoresist AZ5214E was applied in an ultrasonic bath for 10 min at 30 °C, rinsed with isopropanol for 1 min and spin-coated at 6000 rpm for 1 min with constant N<sub>2</sub> flow. After degassing at 400 °C for 10 min, the sample was annealed at 900 °C for 30 min in vacuum and cooled down to room temperature. Subsequently, sublimation growth was carried out at 1200 °C for 10 min and 1450 °C for 5 min in Ar at atmospheric pressure. The SiCrystal wafer pieces were first etched in molecular hydrogen at 1550 °C and near ambient pressure<sup>[56]</sup> to remove residual polishing scratches, while BL was grown by heating to around 1465 °C for 4 min under 800 mbar Ar atmosphere.<sup>[40]</sup> Prior to intercalation, the BL was degassed at 600 °C and intercalation of Pb was performed in two different ways: i) deposition of approx. five to ten layers of Pb onto BL/SiC(0001) at room temperature and annealing to 500 °C for 5 min and 700 °C for 3 min afterwards<sup>[24,26]</sup> or ii) deposition of ten layers of Pb followed by post-annealing steps comparable to [25] up to

400 °C. On the samples used particularly for band structure measurements, Pb intercalation was carried out as in [25]. We found that for recipe i), performing only one adsorption/annealing cycle results in an incomplete intercalation. However, by repeating the Pb-adsorption/annealing cycle five times, a significant increase of the homogeneity could be achieved.

**Scanning Tunneling Microscopy and Electron Diffraction:** The surface structures were analyzed by SPA-LEED and scanning tunneling microscopy (STM) at 80 K and 4 K, respectively. Local tunneling spectroscopy (STS) was conducted with a lock-in amplifier at 800 Hz with a modulation voltage of 4 meV.

**X-Ray Photoelectron Spectroscopy:** Measurements were performed using Al K $\alpha$  ( $h\nu = 1486.6$  eV) radiation from a Specs XR50M x-ray source monochromatized with a Specs Focus 500 monochromator. The core level data were taken at a pass energy of  $E_{\text{pass}} = 10$  eV. The photoelectrons were detected using a 2D CCD detector equipped to a Specs Phoibos 150 analyzer. If not mentioned otherwise, all measurements were conducted at room temperature.

**Normal Incidence X-ray Standing Wave:** Experiments were carried out at the I09 beamline of Diamond Light Source Ltd., Didcot, UK. For NIXSW, the sample was aligned in the x-ray beam in a way that the Bragg condition for a certain reflection  $H = (hkl)$  was fulfilled. The photon energy was then scanned through this Bragg condition in a narrow energy range (in our case  $\pm 1.5$  eV at a photon energy of  $E_{\text{Bragg}} = 2458.3$  eV). During this scan, at each and every photon energy, the x-ray intensity of the Bragg diffracted beam (the so-called reflectivity) and a photoelectron spectrum of the relevant atomic species were recorded, in this case the C 1s, Si 2s, and Pb 4f states. At beamline I09, a Scienta EW4000 HAXPES hemispherical electron analyzer records electrons emitted in the angular range from 60° – 90° with respect to the incoming x-ray beam. All data were collected at room temperature. Note that owing to principal geometric restrictions the experiments cannot be performed at normal incidence (of the x-ray beam) precisely, but a small deviation (3.5° in our case) from these ideal conditions must be applied. This was necessary since the back-diffracted x-ray beam had to be separated from the incoming x-ray beam.<sup>[57]</sup> From the photoelectron spectra, the partial yield curves of all relevant species were extracted using CASAXPS.<sup>[58]</sup> The resulting yield curves, together with the reflectivity, were further analyzed using the dedicated software TORRICELLI.<sup>[38,59]</sup> In this analysis, the structural parameters coherent fraction  $F_c^H$  and coherent position  $P_c^H$  were obtained for each individual measurement. Both parameters range from 0 to 1. While  $P_c^H$  represents the average vertical position  $z$  of the atoms,  $F_c^H$  was a parameter reflecting their vertical order.  $F_c^H = 1$  was achieved if all atoms of the considered species were located at the same distance to the Bragg planes of the  $(hkl)$  reflection used, while smaller values reflect vertical disorder or multiple heights. For more details of the NIXSW method and its data analysis please refer to Refs. [38, 57, 60, 61].

**ARPES:** Band structure investigations were done using angle-resolved photoelectron spectroscopy (ARPES) carried out at the BLOCH beamline of the MAX IV synchrotron facility in Lund. The ARPES spectra were measured using a high performance deflector-based DA30 hemispherical analyzer from Scienta Omicron at a sample temperature of 20 K. The energy resolution and approximate spot size were set to 30–50 meV and  $20 \times 12 \mu\text{m}^2$  for the Pb band and to 18 meV and  $12 \times 8 \mu\text{m}^2$  for the Dirac cone measurements.

## Acknowledgements

This work was supported by the DFG within the Research Unit FOR5242 (Ku 4228/1-1, Sta 315/13-1, Se1087/16-1, and Te386/22-1). M.H., S.Wen., F.S.T., F.C.B. and C.K. acknowledge funding by the DFG through the SFB 1083 Structure and Dynamics of Internal Interfaces (project A12). The authors thank Diamond Light Source for the access to the I09 beamline (proposals SI26188-2 and SI33755-1) that contributed to the results presented here, and the I09 beam-line staff, in particular T.-L. Lee and D.A. Duncan for their support during the experiment. The authors acknowledge MAX IV Laboratory for time on Beamline BLOCH under Proposal 20210067, and

also the beamline staff for their support. Research conducted at MAX IV, a Swedish national user facility, was supported by the Swedish Research council under contract 2018-07152, the Swedish Governmental Agency for Innovation Systems under contract 2018-04969, and Formas under contract 2019-02496.

Open access funding enabled and organized by Projekt DEAL.

## Conflict of Interest

The authors declare no conflict of interest.

## Data Availability Statement

The data that support the findings of this study are available from the corresponding author upon reasonable request.

## Keywords

angle-resolved photoelectron spectroscopy, charge-neutral epitaxial graphene, low energy electron diffraction, normal incidence x-ray standing wave, Pb monolayer intercalation, scanning tunneling microscopy, X-ray photoelectron spectroscopy

Received: June 8, 2023  
Published online: July 23, 2023

- [1] K. S. Novoselov, A. K. Geim, S. V. Morozov, D. Jiang, M. I. Katsnelson, I. V. Grigorieva, S. V. Dubonos, A. A. Firsov, *Nature* **2005**, *438*, 197.
- [2] A. H. Castro Neto, F. Guinea, N. M. R. Peres, K. S. Novoselov, A. K. Geim, *Rev. Mod. Phys.* **2009**, *81*, 109.
- [3] Y. Cao, V. Fatemi, S. Fang, K. Watanabe, T. Taniguchi, E. Kaxiras, P. Jarillo-Herrero, *Nature* **2018**, *556*, 43.
- [4] K. S. Novoselov, D. V. Andreeva, W. Ren, G. Shan, *Front. Phys.* **2019**, *14*, 13301.
- [5] C. Li, Y.-F. Zhao, A. Vera, O. Lesser, H. Yi, S. Kumari, Z. Yan, C. Dong, T. Bowen, K. Wang, H. Wang, J. L. Thompson, K. Watanabe, T. Taniguchi, D. Reifsnnyder Hickey, Y. Oreg, J. A. Robinson, C.-Z. Chang, J. Zhu, *Nat. Mat.* **2023**, *22*, 570.
- [6] C. Berger, W. A. de Heer, *Nat. Mat.* **2020**, *19*, 583.
- [7] C. Riedl, C. Coletti, T. Iwasaki, A. A. Zakharov, U. Starke, *Phys. Rev. Lett.* **2009**, *103*, 246804.
- [8] F. Speck, J. Jobst, F. Fromm, M. Ostler, D. Waldmann, M. Hundhausen, H. B. Weber, T. Seyller, *Appl. Phys. Lett.* **2011**, *99*, 122106.
- [9] J. L. McChesney, A. Bostwick, T. Ohta, T. Seyller, K. Horn, J. González, E. Rotenberg, *Phys. Rev. Lett.* **2010**, *104*, 136803.
- [10] S. Ichinokura, K. Sugawara, A. Takayama, T. Takahashi, S. Hasegawa, *ACS Nano* **2016**, *10*, 2761.
- [11] S. Link, S. Forti, A. Stöhr, K. Küster, M. Rösner, D. Hirschmeier, C. Chen, J. Avila, M. C. Asensio, A. A. Zakharov, T. O. Wehling, A. I. Lichtenstein, M. I. Katsnelson, U. Starke, *Phys. Rev. B* **2019**, *100*, 121407.
- [12] P. Rosenzweig, H. Karakachian, S. Link, K. Küster, U. Starke, *Phys. Rev. B* **2019**, *100*, 035445.
- [13] P. Rosenzweig, H. Karakachian, D. Marchenko, K. Küster, U. Starke, *Phys. Rev. Lett.* **2020**, *125*, 176403.
- [14] I. Gierz, T. Suzuki, R. T. Weitz, D. S. Lee, B. Krauss, C. Riedl, U. Starke, H. Höchst, J. H. Smet, C. R. Ast, K. Kern, *Phys. Rev. B* **2010**, *81*, 235408.
- [15] S. Forti, S. Link, A. Stöhr, Y. Niu, A. A. Zakharov, C. Coletti, U. Starke, *Nat. Commun.* **2020**, *11*, 2236.
- [16] P. Rosenzweig, U. Starke, *Phys. Rev. B* **2020**, *101*, 201407.
- [17] W. Lee, Y. Wang, W. Qin, H. Kim, M. Liu, T. N. Nunley, B. Fang, R. Maniyara, C. Dong, J. A. Robinson, V. H. Crespi, X. Li, A. H. MacDonald, C.-K. Shih, *Nano Letters* **2022**, *22*, 7841.
- [18] J. Baringhaus, A. Stöhr, S. Forti, U. Starke, C. Tegenkamp, *Sci. Rep.* **2015**, *5*, 9955.
- [19] V. Yeh, M. Yakes, M. Hupalo, M. C. Tringides, *Surf. Sci.* **2004**, *562*, L238.
- [20] A. Yurtsever, J. Onoda, T. Iimori, K. Niki, T. Miyamachi, M. Abe, S. Mizuno, S. Tanaka, F. Komori, Y. Sugimoto, *Small* **2016**, *12*, 3956.
- [21] S. Chen, P. A. Thiel, E. Conrad, M. C. Tringides, *Phys. Rev. Mat.* **2020**, *4*, 124005.
- [22] T. Hu, D. Yang, H. Gao, Y. Li, X. Liu, K. Xu, Q. Xia, F. Ma, *Carbon* **2021**, *179*, 151.
- [23] J. Wang, M. Kim, L. Chen, K.-M. Ho, M. Tringides, C.-Z. Wang, S. Wang, *Phys. Rev. B* **2021**, *103*, 085403.
- [24] M. Gruschwitz, C. Ghosal, T.-H. Shen, S. Wolff, T. Seyller, C. Tegenkamp, *Materials* **2021**, *14*, 7706.
- [25] B. Matta, P. Rosenzweig, O. Bolkenbaas, K. Küster, U. Starke, *Phys. Rev. Res.* **2022**, *4*, 023250.
- [26] C. Ghosal, M. Gruschwitz, J. Koch, S. Gemming, C. Tegenkamp, *Phys. Rev. Lett.* **2022**, *129*, 116802.
- [27] Y. Han, M. Kolmer, M. C. Tringides, J. W. Evans, *Carbon* **2023**, *205*, 336.
- [28] C. Kumpf, O. Bunk, J. Zeysing, M. Nielsen, M. Nielsen, R. Johnson, R. Feidenhans'l, *Surf. Sci. Lett.* **2000**, *448*, L213.
- [29] T. Zhang, P. Cheng, W.-J. Li, Y.-J. Sun, G. Wang, X.-G. Zhu, K. He, L. Wang, X. Ma, X. Chen, Y. Wang, Y. Liu, H.-Q. Lin, J.-F. Jia, Q.-K. Xue, *Nat. Phys.* **2010**, *6*, 104.
- [30] C. Tegenkamp, Z. Kallassy, H. Pfnür, H.-L. Günter, V. Zielasek, M. Henzler, *Phys. Rev. Lett.* **2005**, *95*, 176804.
- [31] C. Brand, H. Pfnür, G. Landolt, S. Muff, J. H. Dil, T. Das, C. Tegenkamp, *Nat. Commun.* **2015**, *6*, 8118.
- [32] L. Seehofer, G. Falkenberg, D. Daboul, R. L. Johnson, *Phys. Rev. B* **1995**, *51*, 13503.
- [33] S. Stepanovsky, M. Yakes, V. Yeh, M. Hupalo, M. C. Tringides, *Surf. Sci.* **2006**, *600*, 1417.
- [34] M. Yakes, V. Yeh, M. Hupalo, M. C. Tringides, *Phys. Rev. B* **2004**, *69*, 224103.
- [35] T.-L. Chan, C. Z. Wang, M. Hupalo, M. C. Tringides, Z.-Y. Lu, K. M. Ho, *Phys. Rev. B* **2003**, *68*, 045410.
- [36] X.-Y. Ren, H.-J. Kim, S. Yi, Y. Jia, J.-H. Cho, *Phys. Rev. B* **2016**, *94*, 075436.
- [37] E. Speiser, A. Baumann, S. Chandola, N. Esser, M. Zahedifar, P. Kratzer, C. Tegenkamp, *Phys. Rev. B* **2018**, *98*, 195427.
- [38] F. Bocquet, G. Mercurio, M. Franke, G. van Straaten, S. Weiß, S. Soubatch, C. Kumpf, F. Tautz, *Comp. Phys. Commun.* **2019**, *235*, 502.
- [39] M. Kruskopf, D. M. Pakdehi, K. Pierz, S. Wundrack, R. Stosch, T. Dziomba, M. Götz, J. Baringhaus, J. Aprojanz, C. Tegenkamp, J. Lidzba, T. Seyller, F. Hohls, F. J. Ahlers, H. W. Schumacher, *2D Mater.* **2016**, *3*, 041002.
- [40] K. V. Emtsev, A. Bostwick, K. Horn, J. Jobst, G. L. Kellogg, L. Ley, J. L. McChesney, T. Ohta, S. A. Reshanov, J. Röhl, E. Rotenberg, A. K. Schmid, D. Waldmann, H. B. Weber, T. Seyller, *Nat. Mat.* **2009**, *8*, 203.
- [41] J. Sforzini, P. Hapala, M. Franke, G. van Straaten, A. Stöhr, S. Link, S. Soubatch, P. Jelinek, T.-L. Lee, U. Starke, M. Švec, F. C. Bocquet, F. S. Tautz, *Phys. Rev. Lett.* **2016**, *116*, 126805.
- [42] P. Pyykkö, M. Atsumi, *Chemistry – A European J.* **2009**, *15*, 186.
- [43] A. Bondi, *J. Phys. Chem.* **1964**, *68*, 441.
- [44] A. C. Qu, P. Nigge, S. Link, G. Levy, M. Michiardi, P. L. Spandar, T. Mattheß, M. Schneider, S. Zhdanovich, U. Starke, C. Gutiérrez, A. Damascelli, *Sci. Adv.* **2023**, *8*, eabm5180.



- [45] K. V. Emtsev, F. Speck, T. Seyller, L. Ley, J. D. Riley, *Phys. Rev. B* **2008**, 77, 155303.
- [46] G. D. Mahan, *Phys. Rev. B* **1975**, 11, 4814.
- [47] A. Van Bommel, J. Crombeen, A. Van Tooren, *Surface Science* **1975**, 48, 463.
- [48] C. J. Karlsson, E. Landemark, Y.-C. Chao, R. I. G. Uhrberg, *Phys. Rev. B* **1992**, 45, 6321.
- [49] W. Y. Yang, H. Iwakuro, H. Yagi, T. Kuroda, S. Nakamura, *Japanese Journal of Applied Physics* **1984**, 23, 1560.
- [50] P. De Padova, C. Quaresima, P. Perfetti, B. Olivieri, C. Leandri, B. Aufray, S. Vizzini, G. Le Lay, *Nano Letters* **2008**, 8, 271.
- [51] J. Ristein, S. Mammadov, T. Seyller, *Phys. Rev. Lett.* **2012**, 108, 246104.
- [52] S. Mammadov, J. Ristein, R. J. Koch, M. Ostler, C. Roidel, M. Wanke, R. Vasiliauskas, R. Yakimova, T. Seyller, *2D Mat.* **2014**, 1, 035003.
- [53] C. Brand, S. Muff, M. Fanciulli, H. Pfnür, M. C. Tringides, J. H. Dil, C. Tegenkamp, *Phys. Rev. B* **2017**, 96, 035432.
- [54] N. Sieber, T. Seyller, R. Graupner, L. Ley, R. Mikalo, P. Hoffmann, D. Batchelor, D. Schmeißer, *Applied Surface Science* **2001**, 184, 278.
- [55] M. Ostler, F. Speck, M. Gick, T. Seyller, *physica status solidi (b)* **2010**, 247, 2924.
- [56] S. Soubatch, S. E. Sadow, S. P. Rao, W. Y. Lee, M. Konuma, U. Starke, *Mater. Sci. Forum* **2005**, 483, 761.
- [57] G. van Straaten, M. Franke, F. C. Bocquet, F. S. Tautz, C. Kumpf, *J. Elec. Spec. Relat. Phen.* **2018**, 222, 106.
- [58] N. Fairley, CasaXPS, version 2.3.19pr1.0, casa software ltd.
- [59] The latest version of the open-source software Torricelli is available at [www.torricelli-software.com](http://www.torricelli-software.com).
- [60] (Eds.: J. Zegenhagen, A. Kazimirov), *The X-Ray Standing Wave Technique*, World Scientific, Singapore **2013**.
- [61] D. P. Woodruff, *Rep. Prog. Phys.* **2005**, 68, 743.